Unlocking onshore imaging challenges with FWI: Case studies from the Sultanate of Oman

Yonghe Guo[1], Ahmed Aziz[1], Anna Sedova[2], Mathieu Reinier[2], Daniela Donno[2], Gilles Lambaré[2], and Diego Carotti[2]

https://doi.org/10.1190/tle44010022.1

Abstract

Velocity model building and depth imaging are known to be complicated endeavors in numerous onshore areas in the Middle East. Despite recent advancements toward denser, wide-azimuth, and low-frequency seismic acquisitions, the application of full-waveform inversion (FWI) remains challenging. The main difficulties arise from complex near-surface geology that creates wave mode conversions (P to S waves but also strong multiples) and very energetic and complex ground roll overlaying reflected waves and dominating low frequencies, with the diving waves being less energetic and noisier. This paper presents recent progress in land FWI toward higher-resolution velocity models, with successful applications to case studies from the Sultanate of Oman. The first example shows an application of land FWI imaging. It shows that we are able to invert jointly diving and reflected waves in acoustic FWI. With proper input data conditioning and initial model preparation, we successfully ran acoustic FWI up to 45 Hz, resulting in a high-resolution velocity model and derived FWI image that significantly improved subsurface imaging and geologic understanding. The inverted high-frequency velocity could also be more reliably used for subsequent reservoir characterization steps. Given the important role of a good-quality near-surface model for stabilizing high-frequency FWI updates, the second example highlights the creation of a detailed shallow velocity model. We propose using elastic FWI of surface waves for characterization of the near surface in complex geologic settings. Here, we demonstrate the effectiveness of this workflow to enhance imaging of the shallow subsurface. Compared to conventional methods such as surface-wave inversion, elastic FWI of surface waves has the advantage of 3D full-wavefield modeling with no requirement for picking. Our workflow also benefits from the ultra-low frequencies recovered by interferometry to obtain a more stable deeper update.

Introduction

Velocity model building and depth imaging is a very demanding process for onshore projects in the Middle East. For this reason, land seismic acquisition in the Sultanate of Oman has adopted several technological improvements in recent years. The use of vibrators starting from 1.5 Hz (Mahrooqi et al., 2012; Baeten et al., 2013) provides an improvement in low-frequency content compared to conventional vibrators starting from 6 or 8 Hz. Moreover, high-density nodal geophones not only increase the stacking signal-to-noise ratio (S/N), they also record longer offsets and wide-azimuth (WAZ) geometries. The recent use of continuous recordings in blended acquisition surveys (Zhao et al., 2018) enables the opportunity to reconstruct ultra-low-frequency surface waves through interferometry of natural and ambient noise (Le Meur et al., 2020). These technologies provide better seismic input for full-waveform inversion (FWI). However, despite these improvements in the recorded data, FWI still struggles with challenges in the region. First, ground roll dominates the low-frequency energy where diving waves are very weak. Also, while high-density and high-fold acquisitions improve the stack image, single-node traces are noisier than conventional geophone group traces. Simultaneous shooting may further add interference noise that particularly affects the low-frequency S/N, where the blended noise appears coherent. Second, the geologically complex, laterally and vertically, heterogeneous near surface not only generates strong noise (elastic wave mode conversions and multiples), it also makes near-surface velocity estimation particularly challenging.

This paper highlights recent progress and breakthroughs in land FWI with two examples from the Sultanate of Oman (one from the north and one from the south, as shown in Figure 1). Specifically, we focus on two key achievements. First, the utilization of diving and reflected waves in acoustic FWI achieves high-frequency high-resolution velocity models and produces the FWI image (Zhang et al., 2020), which significantly enhances subsurface imaging and geologic understanding (Guo and Aziz, 2024). Second, recent advances in near-surface velocity model building, notably through elastic FWI of surface waves (Sedova et al., 2024), enable the creation of a shallow initial model that contributes to stabilizing the application of FWI for P-wave velocity inversion.

One of the early applications of land acoustic FWI in Oman using low-frequency diving waves to achieve a good long-wavelength velocity update was illustrated by Stopin et al. (2014). Later, several studies demonstrated the value of multiwave inversion (MWI) (Bardainne, 2018) to enhance the initial near-surface model and diving-wave FWI (Farooqui et al., 2021; Masclet et al., 2021) to further improve the shallow velocity resolution in areas with strong shallow vertical velocity contrasts. The first examples of achieving high-frequency land FWI (Sedova et al., 2019; Hermant et al., 2020) presented a workflow for initially inverting diving and refracted waves using a data mute and then inverting conventional depth migration preconditioned data tailored to enhancing reflection energy. The first step updated the

Manuscript received 15 August 2024; revision received 2 October 2024; accepted 16 October 2024.
[1]Viridien, Muscat, Oman. E-mail: yonghe.guo@viridiengroup.com; ahmed.aziz@viridiengroup.com.
[2]Viridien, Massy, France. E-mail: anna.sedova@viridiengroup.com; mathieu.reinier@viridiengroup.com; daniela.donno@viridiengroup.com; gilles.lambare@viridiengroup.com; diego.carotti@viridiengroup.com.

Figure 1. Satellite map of the Sultanate of Oman showing the locations of the two study areas (blue squares).

background velocity, and the reflections added details. The fact that in these workflows the long-offset diving waves are not retained throughout the inversion process may alter the long-wavelength components of the velocity model when pushing FWI to higher frequencies. While still challenging for land data, successful applications of FWI with marine data, even in geologically complex regions, are well established (Wang et al., 2019). There are numerous examples of detailed velocity models and FWI imaging obtained with high-frequency FWI in both shallow and deep water for various geologic challenges (Zhang et al., 2020). These results have enabled the interpretation of complex structures, such as those in salt regions (Huang et al., 2021), and can be used for shallow hazards (Espin et al., 2023). In this paper, we show that these advances toward high-frequency FWI imaging can be applied to land data with proper handling of the input data conditioning and a good starting velocity model.

The near surface in the Middle East, particularly in the Sultanate of Oman, is characterized by very shallow fast carbonates and anhydrites interleaved by slow-velocity clastic layers, resulting in sharp velocity inversions in the first few hundred meters below the surface (Forbes et al., 2010). This complex geology creates strong wave mode conversions and multiples. Acoustic FWI seems unable to address these very shallow velocity complexities due to inaccurate physics of the modeling. Conventional approaches for near-surface characterization are first-arrival traveltime tomography (Taillandier et al., 2009), surface-wave inversion (Socco and Strobbia, 2004), and joint inversion methods such as MWI (Bardainne, 2018). While MWI can provide reliable velocity models of the near surface by jointly inverting first breaks and surface-wave dispersion curve picks (Donno et al., 2021), its limitations include the use of surface-wave dispersion curves rather than full-waveform information and 1D dispersion curve modeling (Socco and Strobbia, 2004). Surface waves (i.e., ground roll) represent the strongest recorded energy for most of the land data sets in Oman, reaching up to 95% of the total recorded energy. While often treated as noise during processing, these waves contain useful near-surface information. Elastic FWI of surface waves can be considered a better choice for characterization of the near surface in complex geology settings because it leverages 3D full-wavefield modeling and can handle all surface-wave modes simultaneously with no requirement for picking. Furthermore, the use of surface waves in elastic FWI does not suffer from parameter crosstalk between V_P and V_S, as surface-wave propagation depends almost exclusively on V_S. While elastic FWI of surface waves is not a new topic in academia (Pérez Solano et al., 2014; Borisov et al., 2018), it has only recently been investigated in the oil and gas industry by Leblanc et al. (2022) with virtual data built by interferometry (Le Meur et al., 2020) using continuous recording and by Adwani et al. (2022) by inverting surface waves from active deblended data. We present an application of elastic FWI of surface waves for near-surface characterization, which provides detailed and valuable information for velocity model building.

Moving toward high-resolution FWI and FWI imaging

The study area is located in the gravel plain in the northern part of the Sultanate of Oman (Figure 1) that lies between the mountains and the desert area. One of the exploration targets of this area is regional fault-related structures, as shown in Figure 2a. The legacy result failed to resolve the horizontal and vertical velocity variations. Encouraged by the successes and benefits of marine FWI imaging, particularly in terms of sharp faulting resolution, we implemented FWI imaging in this land data case study. The data for this survey were acquired in 2022 with vibrators of 1.5–86 Hz sweep frequency and simultaneous shooting with 25 × 25 m shot spacing and 75 × 100 m geophone node spacing. The data for this survey have WAZ coverage with a maximum offset of approximately 13 km. All of the main acquisition parameters are therefore suitable for FWI. Using a smoothed version of the legacy model and the input data geometry, we also analyzed the diving-wave illumination because it is well known that the diving wave is the main driving force for FWI. From the result in Figure 2a, we can see that the maximum penetration depth of the diving waves is limited by the presence of strong velocity inversion at a depth between 2 and 4 km, and the diving waves can well sample the main fault structure.

After deblending (Guillouet et al., 2016), the low-frequency signal (1–6 Hz) was still noisy (Figure 2b), only enabling identification of ground roll. This was the only coherent signal visible at this stage, with diving and reflected waves being much weaker

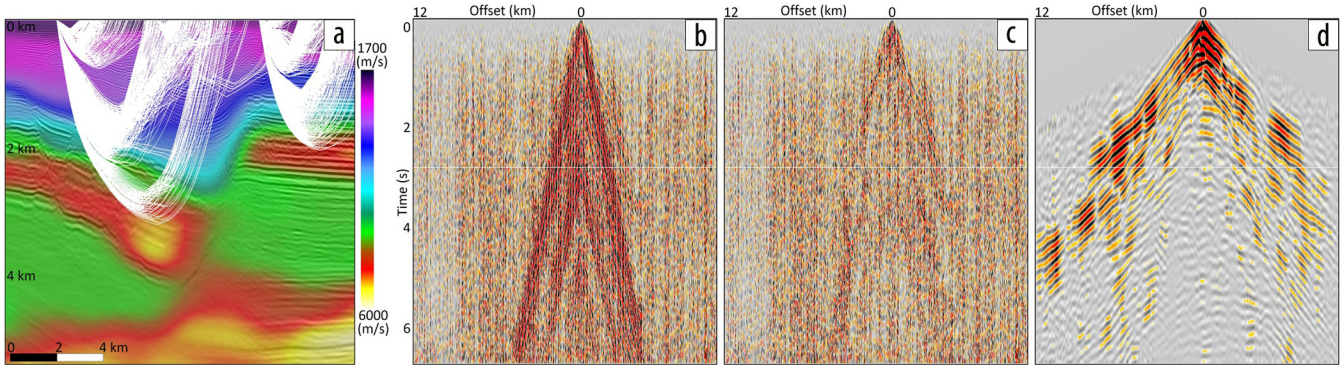

Figure 2. (a) The initial V_p velocity model overlaid on migrated seismic stack. The diving-wave illumination analysis shows that the penetration depth of diving waves is limited by the presence of the layer with strong velocity inversion between 2 and 4 km depth. (b) Receiver gather after deblending with a low-pass filter at 6 Hz (c) after matching-pursuit linear radon surface-wave attenuation and (d) after further advanced denoising by joint low-rank and sparse inversion and remnant linear noise attenuation (a 20 dB gain has been applied to this image).

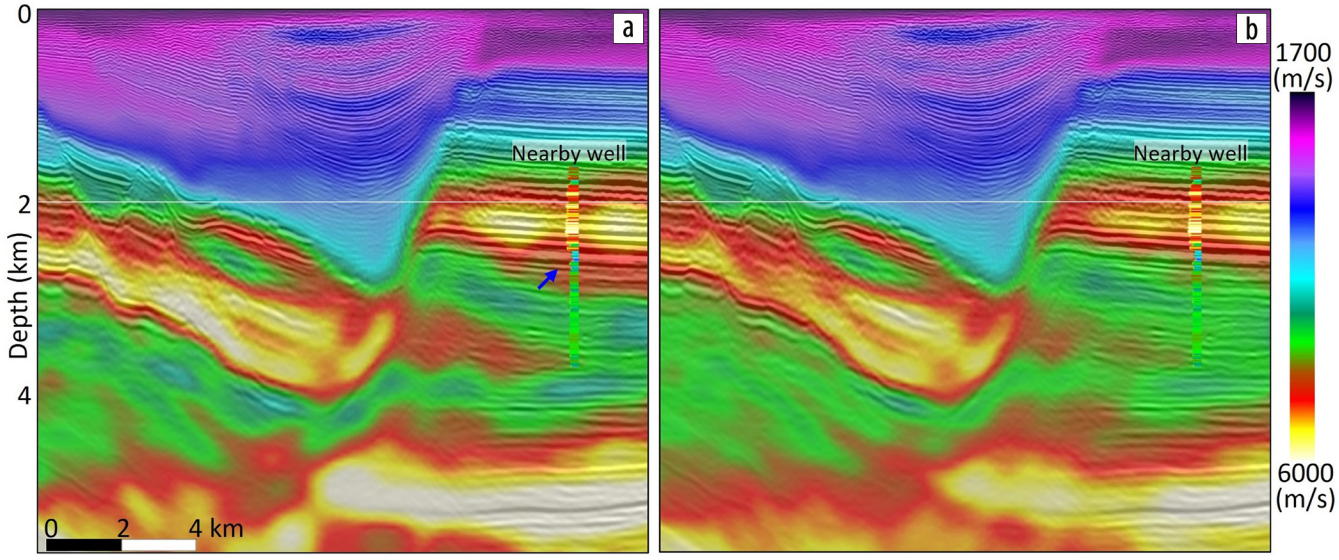

Figure 3. Updated velocity models, overlaid on migrated seismic stack, using input data with different denoising. Results in (a) use data after matching-pursuit linear radon surface-wave attenuation (Figure 2c). Results in (b) use data with advanced denoising (Figure 2d). The QC well is about 10 km away and is only shown here for reference of the major layers.

and obscured by noise. We therefore applied different denoising processes to the input data and analyzed their impact on the FWI velocity. Industry experience of FWI with marine data has shown that denoise is generally not critical for data with a reasonably high sampling density. So, we wanted to see if the same observation applies to land data. Because acoustic FWI was used for high-frequency FWI imaging, the ground roll needed to be removed. Matching-pursuit linear radon surface-wave attenuation (Ng and Perz, 2004) was initially used to remove the strong ground roll. The result in Figure 2c shows that the strong ground roll has been attenuated without obvious signal leakage. However, after ground-roll attenuation, we can still hardly see the signal from diving waves and reflections. For this reason, we further cleaned the input data with (1) a 4D joint low-rank and sparse inversion (Sternfels et al., 2015) to attenuate the random noise and (2) a linear-noise attenuation method (Le Meur et al., 2008) to remove any residual ground roll and linear noise. The receiver gather in Figure 2d is much cleaner, and the weak diving waves and reflections, that were indeed recorded by the nodes, are now visible after applying a 20 dB gain. We ran FWI from 2.5 to 6 Hz using these two input data sets without any data mute. The minimum reliable frequency of 2.5 Hz to start FWI was chosen using the phase ring stability QC, as shown in Messud et al. (2021). The updated velocity model using the noisier data set (Figure 3a) looks stable within the diving-wave illumination area and matches the nearby sonic well log. Then, it becomes less stable and deviates from the sonic velocity trend below the velocity inversion, as indicated by the blue arrow. The updated velocity model using data with more advanced preconditioning (Figure 3b) is very similar within the diving-wave illumination zone, showing that FWI is robust with diving waves to achieve a good velocity update. Moreover, beyond the diving-wave penetration depth, the more advanced denoise helps stabilize the velocity update and match it better with the well sonic trend. Overall, we can observe that even though the individual receiver gathers are noisy, dense and WAZ acquisitions make denoise less critical, especially within the diving-wave illumination zone. Other factors that may influence the velocity update are the acquisition geometry and receiver density. The result shown in Figure 4a was obtained using the available WAZ data, with maximum offset in inline and crossline directions of 12 and 6 km, respectively. When reducing the maximum offset in the crossline direction to only 2 km to simulate a narrow-azimuth (NAZ) acquisition (Figure 4b),

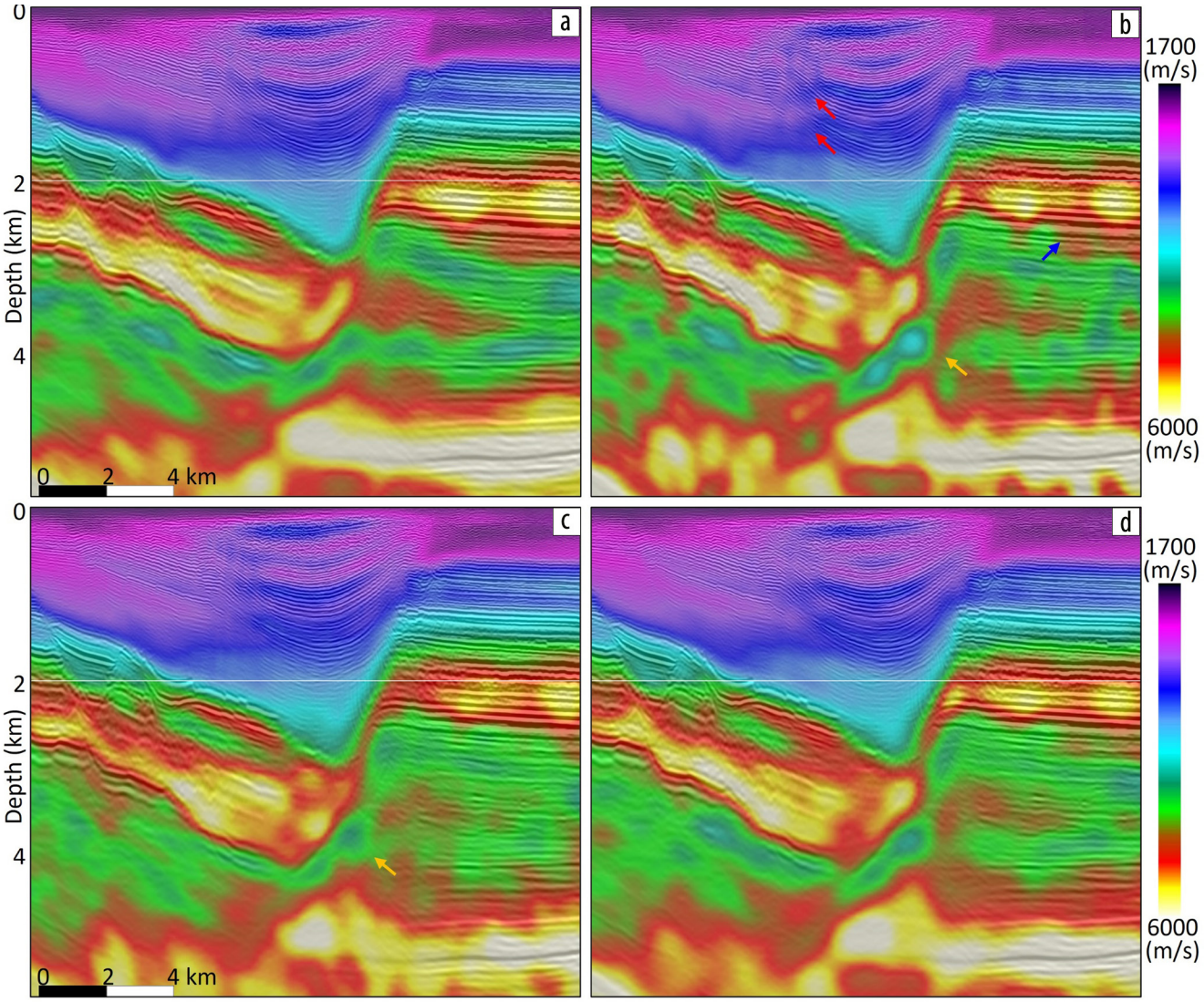

Figure 4. Updated velocity models, overlaid on migrated seismic stack, using input data with different denoising and acquisition geometry parameters: (a) using data after ground-roll attenuation with a WAZ geometry (6 × 12 km offset), (b) using a narrow-azimuth geometry (2 × 12 km offset) compared to (a), (c) using data with advanced denoising compared to (b), and (d) using a denser receiver carpet (75 × 100 m grid) compared to the one (150 × 100 m) used in (b).

we observe that the velocity update in the diving-wave illumination zone starts to be affected by noise as it becomes less conformal to the shallow dipping structures (red arrows). Moreover, the velocity update is more chaotic in the deeper part of the model, below the strong velocity inversion (blue and orange arrows). However, the result after our advanced denoising (Figure 4c) shows a more stable update both in the shallow and deeper part, which indicates that the NAZ geometry acquisition needs more denoise to obtain a stable result. Finally, we also considered a denser receiver grid (75 × 100 m) with the NAZ geometry (Figure 4d) and observe that the use of a denser receiver grid compensates for the noise and stabilizes the update. We can therefore conclude that, in the case of NAZ geometry and sparser receiver density, the impact of denoise is more obvious on the results.

The starting velocity model is another important factor for FWI (Virieux and Operto, 2009). For land data, the near surface is generally very challenging. Among several possible methods proposed in the literature, the near-surface model can be obtained using MWI (Bardainne, 2018). We therefore created two different starting velocity models for FWI and analyzed the impact of the initial model on the result of high-frequency land FWI. The first starting velocity model comes from a legacy project after smoothing (Figure 5a), while the second one in Figure 5b has been obtained by replacing the first 200 m of the near surface with the MWI result for this data set and by improving the deeper part (beyond approximately 2 km depth) with a velocity scan, as indicated by the yellow arrows. After running FWI up to 35 Hz (Figures 5c and 5d) using the two different velocity models, we can observe that FWI is able to achieve a very detailed velocity model that captures both vertical and horizontal velocity variations and well delineates the reverse and smaller fault structures both in the shallow and deep part. However, the result using the legacy starting model (Figure 5c) has fast velocity leakage in the shallow layers, and the deep velocity update is not consistent across the fault, while the result using the improved starting velocity (Figure 5d) is more consistent in both shallow

and deep sections, better matches the well sonic (embedded in Figure 5d), and has higher shallow resolution and reduced ringing. Using the 35 Hz FWI result, we also computed the corresponding FWI image (Zhang et al., 2020) in Figures 5e and 5f. We can see that the FWI image starting from the improved shallow starting model (Figure 5f) gives better shallow reflectivity (red arrows), resulting in less multiple ringing in the deeper part, as indicated by the blue arrows, because multiples are better modeled (we have a free-surface condition in our acoustic modeling) to match the recorded data.

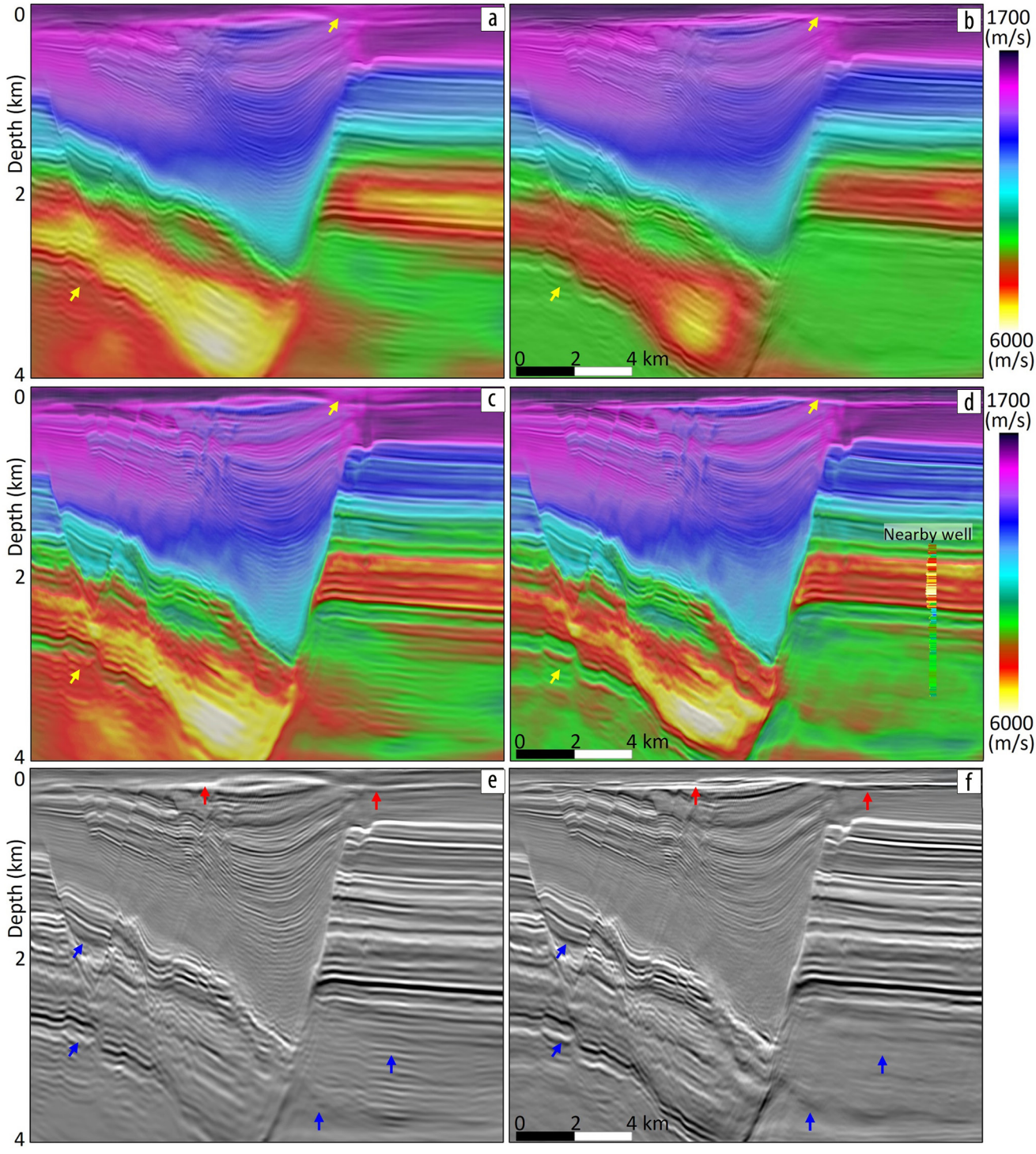

Figure 5. Starting velocity models for FWI coming from a legacy project (a) after replacing the first 200 m with the MWI model and (b) by improving the deeper part with a velocity scan. The corresponding 35 Hz FWI updated velocity models are in (c) and (d). The associated FWI images are in (e) and (f). Note that the overlaid seismic in (a) and (c) is the FWI image in (e), while (b) and (d) show the FWI image in (f). The yellow arrows indicate the locations where modifications from the starting velocity model in the shallow and deep parts are more visible. The red arrows indicate locations with better shallow reflectivity. The blue arrows indicate less multiple ringing in the deeper part when using the starting velocity model in (b). The QC well shown in (d) is about 10 km away and is only shown here for reference of the major layers.

Furthermore, we compared the FWI image in Figure 5f (repeated in Figure 6b for comparison), created from the velocity model inverted by acoustic FWI up to 35 Hz (Figure 5d), with the migrated image using the legacy model. The legacy velocity (Figure 5a) captured the background velocity trend but could not resolve the horizontal and vertical velocity contrasts near the major fault. Indeed, its resolution is not sufficient to obtain a good-quality Kirchhoff-migrated image (Figure 6a). Therefore, we used the input data after premigration demultiple (same input as used in Figure 6a) and the 35 Hz high-resolution FWI velocity model of Figure 5d for the migration, using both Kirchhoff and reverse-time-migration (RTM) algorithms. With such detailed velocity, Kirchhoff migration (Figure 6c) gives an improved image, except at the major fault where the presence of the sharp velocity contrast may not be adapted for the ray-tracing algorithms. RTM better handles the velocity contrast (Figure 6d), as we can observe less swings across the fault and better amplitude compared to the Kirchhoff result. However, the RTM image is still limited by the use of primary-only reflections in such a complex region. Thanks to the utilization of additional diving waves and multiple reflections and the least-squares iterative data fitting from low to high frequencies, the FWI image (Figure 6b) offers significant improvement in the complex fault area, offering a much better geologic understanding of the faulted structures from shallow to 4 km in depth. Enhancement of the shallow fault definition in the top-left part of Figure 6b can also be appreciated by examining a depth slice at 450 m depth (Figure 7). When compared to the Kirchhoff image obtained using the legacy velocity model (Figures 7a and 7b), the complex system of faults is imaged with significantly higher resolution in both the 35 Hz FWI image and velocity model (Figures 7c and 7d, respectively). This improved imaging can be attributed to the additional illumination provided by diving waves in the shallow layers.

The previous examples demonstrate that by employing a dense and WAZ acquisition, adapted preconditioning, and a good starting model, it is possible to obtain a high-frequency land FWI image. To analyze the potential benefits of increasing to an even higher frequency for improved imaging of shallow targets, we applied the same workflow to a nearby area. Figures 8a and 8d show the legacy velocity model and the corresponding Kirchhoff

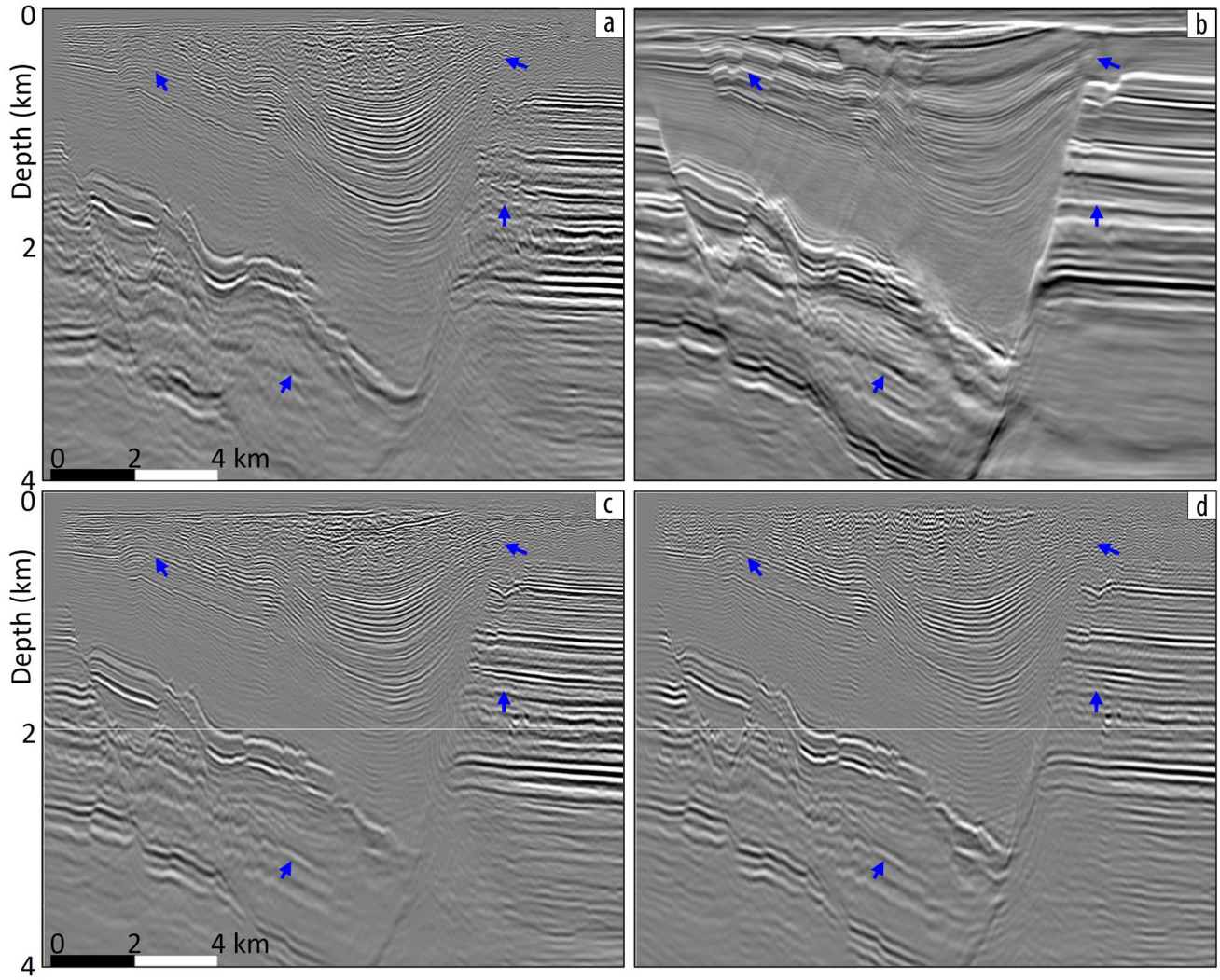

Figure 6. (a) Kirchhoff depth-migrated section using a legacy velocity model. (b) FWI image computed from the 35 Hz acoustic FWI updated velocity. (c) Kirchhoff depth-migrated section using the 35 Hz FWI model. (d) RTM-migrated section using the 35 Hz FWI model. The blue arrows indicate the location with the most significant improvements achieved by the FWI image.

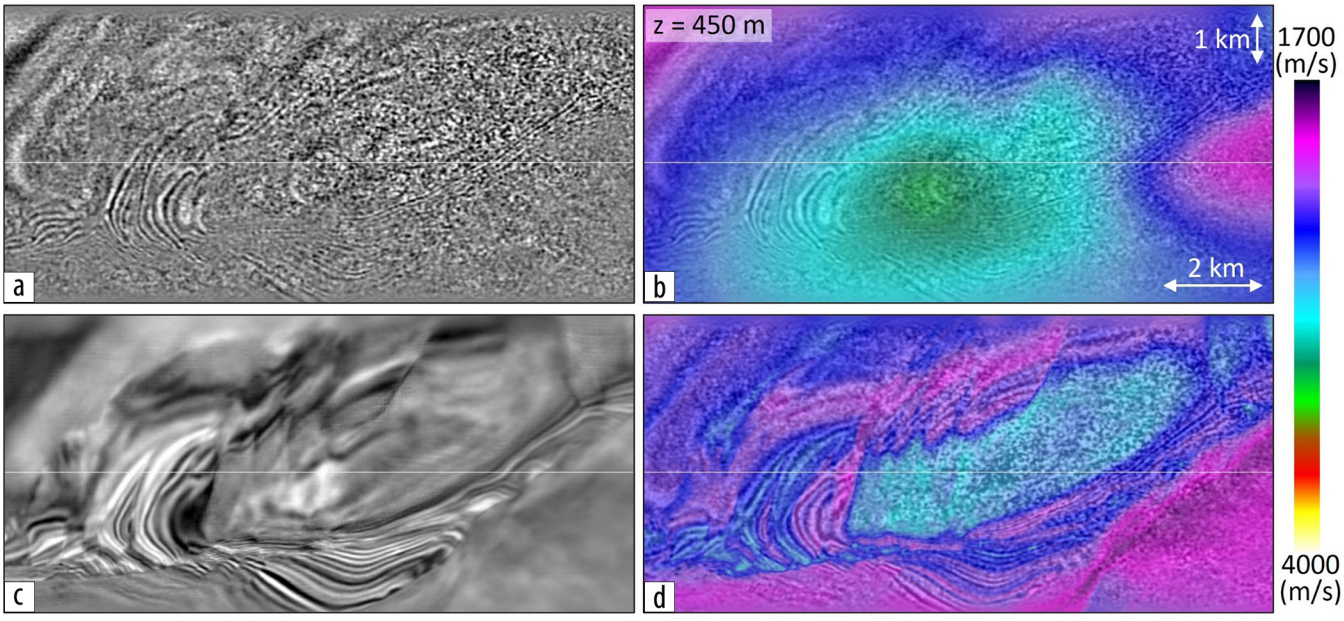

Figure 7. Depth slice at 450 m depth of: (a) Kirchhoff depth migration using legacy velocity model, (b) legacy velocity model, (c) FWI image computed from the 35 Hz acoustic FWI updated velocity, and (d) 35 Hz acoustic FWI updated velocity model.

migration, respectively. We can observe that the legacy velocity is variable across the fault for the layers, and unnecessary undulations are visible in the migrated stack section. The result of the 20 Hz FWI gives a good background velocity model update (Figure 8b), which helps correct the structure undulation if used for Kirchhoff migration. This structural improvement is also visible in the 20 Hz FWI image (Figure 8e) corresponding to the model in Figure 8b. The fault definition (red arrows) is also already very sharp at this low frequency; however, the 20 Hz FWI image has low resolution for the shallow target, indicated by the blue arow. The result of the 45 Hz FWI updated velocity and FWI image (Figures 8c and 8f, respectively) restores the details compared to legacy Kirchhoff migration, including high-resolution imaging of the clinoforms (blue arrow). Overall, FWI imaging shows very clear fault delineation from shallow to deep and produces rich low-frequency content due to the accurate kinematic background velocity. This low-frequency content minimized dependency on the well-interpolated low-frequency model for subsequent reservoir characterization steps.

Elastic FWI of surface waves for near-surface characterization

The previous example illustrated the value of using a high-quality near-surface starting velocity model for FWI imaging of deeper structures. The shallow geology in the southern part of the Sultanate of Oman (Figure 1) features strong vertical and lateral velocity contrasts from layered sands, carbonates, and anhydrites, generating strong elastic effects. Therefore, elastic FWI could be more appropriate for near-surface characterization in the case study presented in this paper. The data set was acquired with a typical dense blended acquisition of vibroseis sources, a minimum frequency of 1.5 Hz, and vertical geophones as receivers. For these data, surface waves account for about 95% of the total recorded energy, making them attractive to exploit. These waves propagate parallel to the earth's surface at a slightly lower velocity than V_S and penetrate down to a depth roughly equal to the S-wave wavelength. By using virtual data reconstructed by interferometry of the ambient noise recorded during blended continuous acquisitions (Le Meur et al., 2020), we can access surface waves with frequencies as low as 0.5 Hz. Incorporating virtual data into our workflow allows us to update the V_S model to greater depths and avoid cycle-skipping issues. Figure 9 shows the comparison of one shot gather at the same location for deblended active data and virtual data obtained by interferometry. The virtual shot gather in Figure 9a is very similar to the active one in Figure 9c, even though the virtual data exhibit lower-frequency content. Figures 9b and 9d are time slices at 2.4 s of virtual and active data, respectively, with a low-pass filter applied at 1.5 Hz, which is the minimum frequency of the active sweep source. The active data in Figure 9d contain no coherent signal, while the reconstructed virtual data contain clear signal (Figure 9b). Moreover, the virtual data exhibit a strong directionality (perpendicular to the coastline in this case), as indicated by the orange arrow in Figure 9b. This dominant direction is attributed to the orientation of ocean waves impacting the shoreline, which likely serve as the primary source generating the low-frequency ambient noise.

The first step of our workflow is elastic FWI (Leblanc et al., 2022) using the ultra-low-frequency virtual data created by 3D interferometry. For the observed input data, we selected the traces of the virtual shot gathers along the azimuth with the dominant energy (orange arrow in Figure 9b). We updated the V_S model by elastic FWI inverting the virtual data from 0.5 to 2 Hz, starting from very smooth regional velocities (Figure 10a). This step provided a long-wavelength V_S update down to nearly 2 km. In the second step, the V_S model was updated by elastic FWI of the ground roll from the active data from 2 to 7 Hz. It provided a detailed shallow V_S model characterized by both lateral and vertical velocity variations (Figure 10c). The data-fit QC in Figures 10b and 10d, obtained by overlaying the observed and

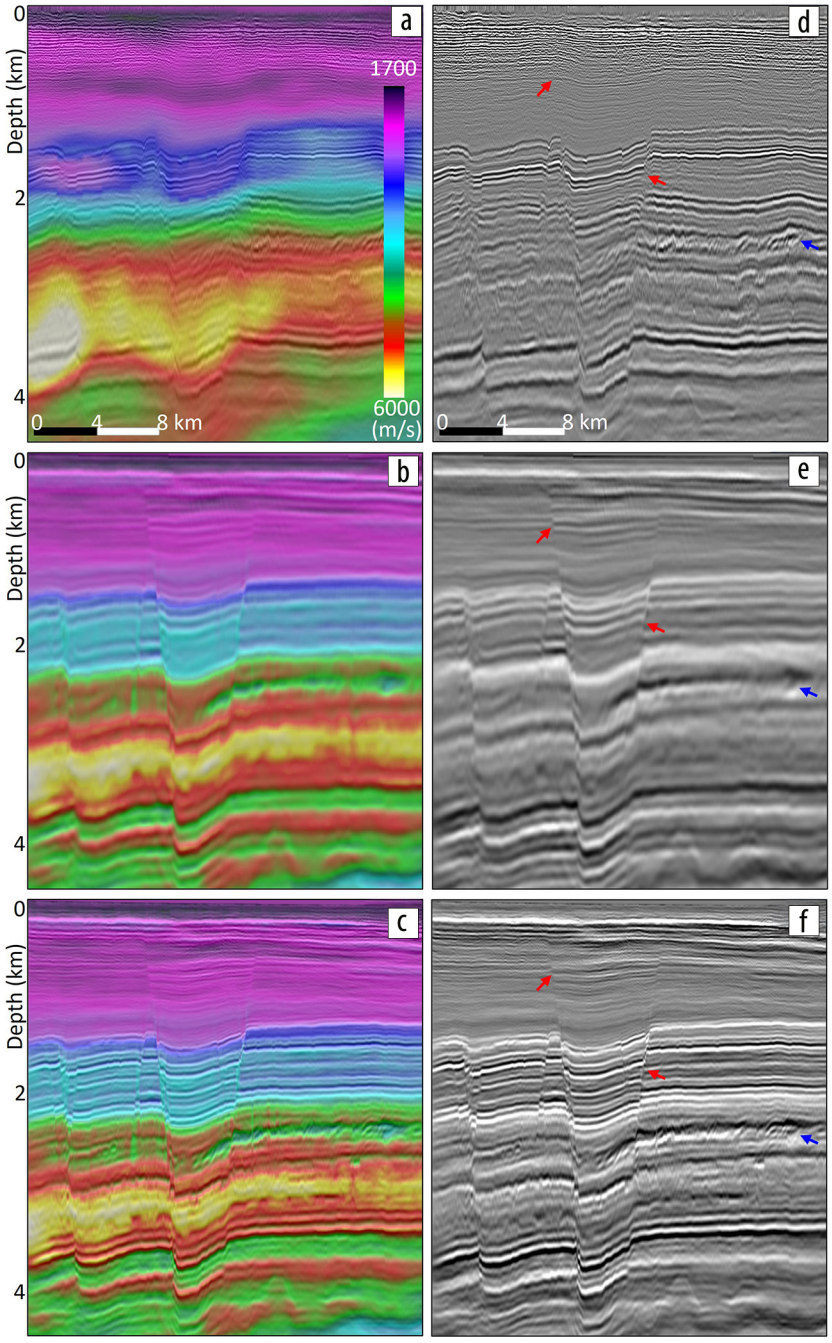

Figure 8. (a) Legacy velocity model overlaid on migrated seismic stack and (d) corresponding Kirchhoff depth migration. (b) The 20 Hz FWI updated velocity model overlaid on FWI image and (e) corresponding 20 Hz FWI image. (c) The 45 Hz FWI updated velocity model overlaid on FWI image and (f) corresponding 45 Hz FWI image. The red and blue arrows indicate the improved resolution obtained by the FWI image.

modeled data, shows that we were able to successfully fit not only the surface waves but also later reflection arrivals, corresponding to S-S reflections (yellow arrows in Figure 10d). These energetic reflections are likely generated by strong velocity contrasts in both the shallow and deeper sections (Figure 10c). Figures 11a and 11c show a depth slice 150 m below the surface of the legacy V_S model (obtained with MWI in the shallow part) and the associated migrated image. The corresponding depth slice of the V_S updated by elastic FWI of surface waves up to 7 Hz (Figure 11b) displays high-resolution velocity variations that correlate with shallow features (indicated by the red arrows in Figure 11) visible in the migrated depth slice and satellite image (Figure 11d). These features were not detected by the conventional model building workflow (Figure 11a). The advantages of elastic FWI of surface waves are (1) it requires minimal data preprocessing (as surface waves are the strongest energy) and (2) it takes advantage of the ultra-low frequencies of virtual data to obtain high-resolution velocity updates. In contrast, MWI relies on a simplified physics and a more complex and cumbersome workflow.

In this study, we integrated the V_S model obtained by elastic FWI into a conventional V_P velocity model building workflow by scaling the first 500 m of the inverted V_S model by a constant V_P/V_S ratio, ensuring the calibration of P-P reflections with the well markers. The resulting shallow V_P model was combined with the legacy V_P model, and a pass of global tomography below 500 m ensured seamless integration of the shallow update into the legacy velocity model. The results of the described workflow are shown in Figure 12. For comparison, the data were migrated with the legacy V_P model (obtained with the combination of MWI, acoustic FWI, and reflection tomography) and with the proposed approach integrating the scaled V_S model into the legacy V_P model. The migrated inline section indicated by the black line in Figure 11 is shown in Figure 12. We note that the shallow velocity variations help flatten the shallow reflections and simplify the geologic structures. The red arrows in Figure 12d indicate the position of the base of the high-velocity anhydrite Rus Formation, typical of this region at shallow depth, which marks a strong vertical velocity contrast. This reflector is flattened and more continuous along the whole section with the proposed approach.

Conclusions

FWI using marine data is a well-established technology, with numerous examples of detailed high-frequency velocity models and FWI images solving various challenges in both shallow and deep water. However, application of FWI remains more challenging for land data, despite the recent progress of

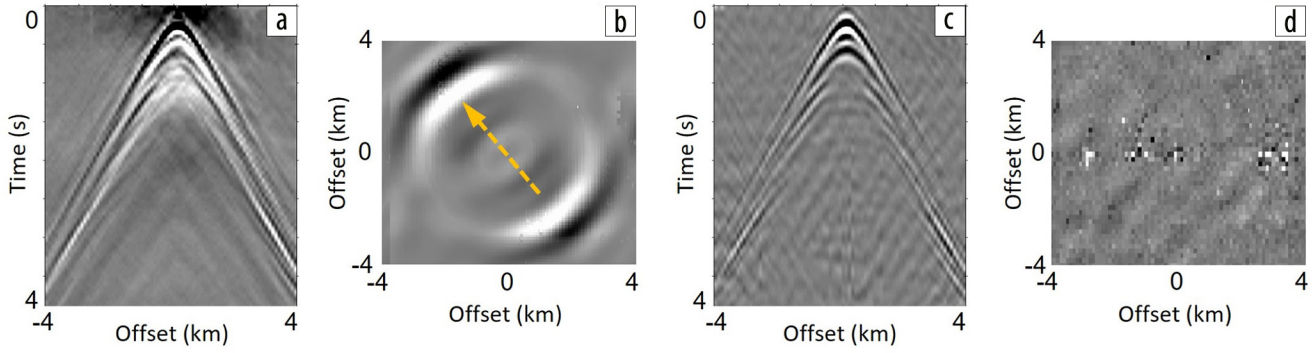

Figure 9. Virtual data from interferometry: (a) shot gather and (b) time slice at 2.4 s with a low-pass filter at 1.5 Hz. The orange arrow indicates the dominant direction of interferometry-reconstructed data. Active deblended data: (c) shot gather and (d) time slice at 2.4 s with a low-pass filter at 1.5 Hz.

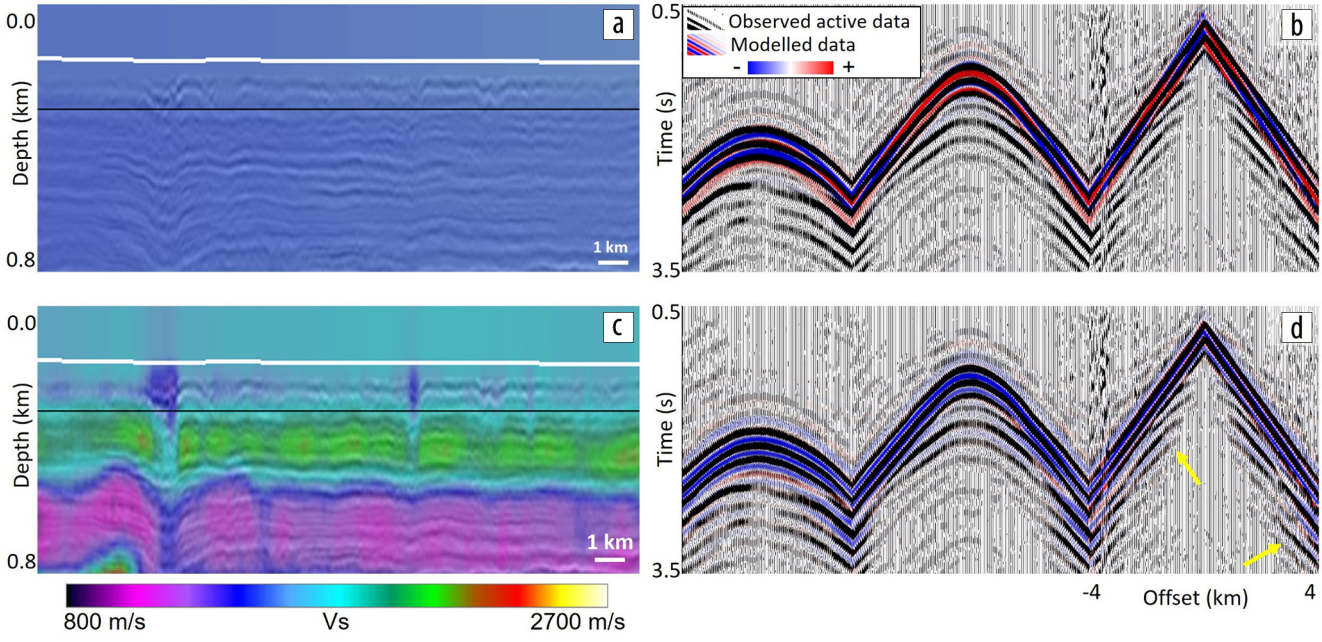

Figure 10. (a) Initial V_S model and (b) corresponding data-fit QC at 7 Hz between elastic modeled data and observed active data. (c) The 7 Hz V_S elastic FWI updated model and (d) corresponding data-fit QC at 7 Hz between elastic modeled data and observed active data.

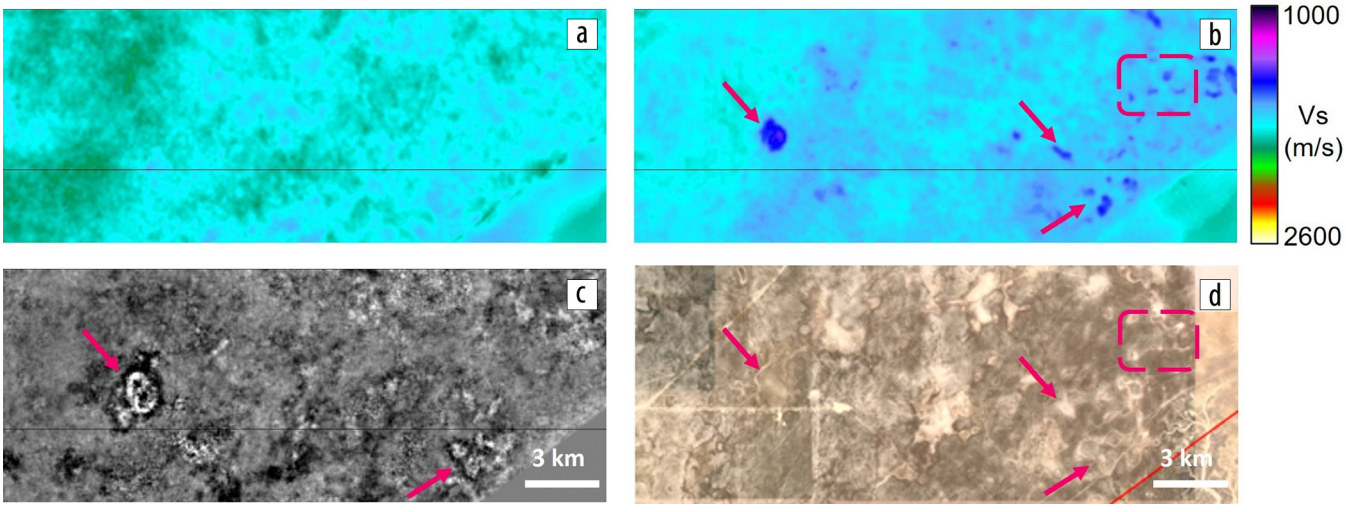

Figure 11. Depth slice at 150 m depth of the V_S model obtained with (a) MWI and (b) elastic FWI of surface waves. (c) Depth slice at 150 m of the reference migration using MWI velocity. (d) Satellite image of the same area.

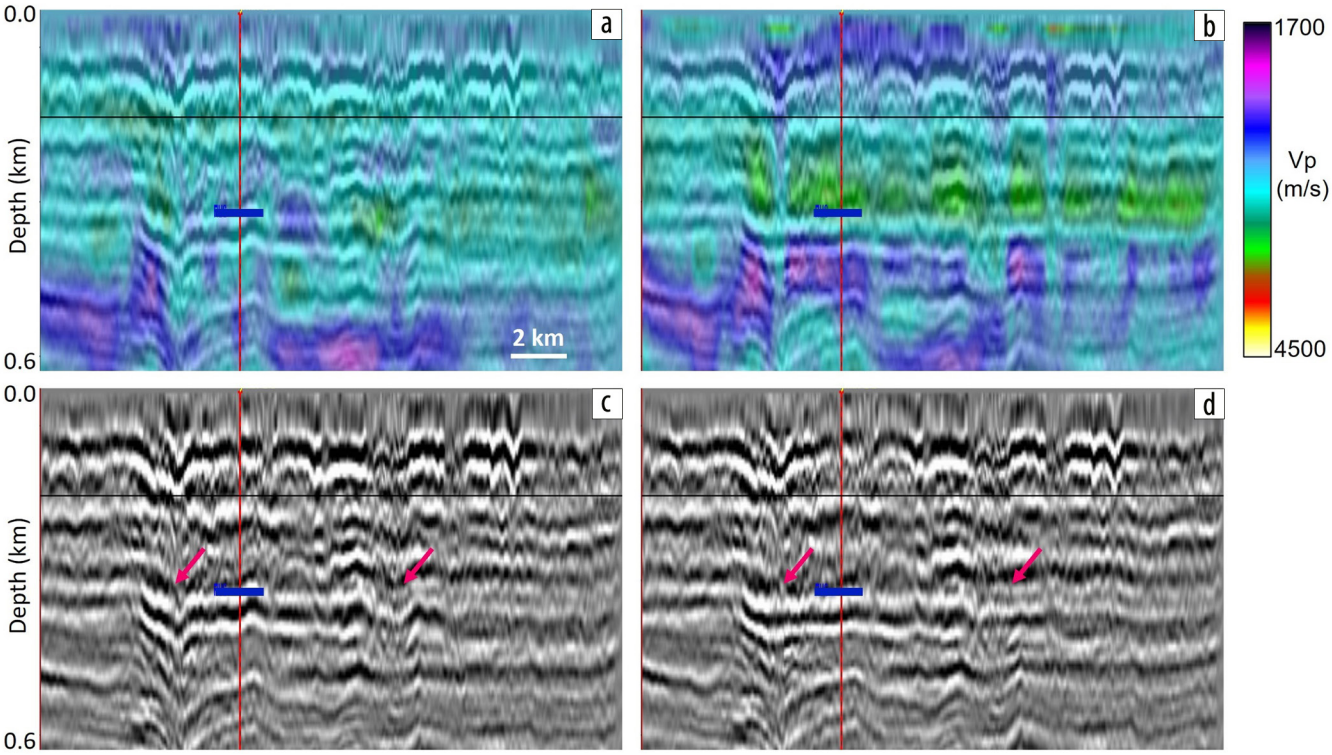

Figure 12. Shallow section (a) before and (b) after integration of the scaled V_S elastic FWI model in the legacy migration model, with the associated PP-migrated stack sections in (c) and (d), respectively. The red vertical line represents the location of a well, with a formation marker in blue.

onshore seismic acquisitions. In this paper, we presented two successful applications of land FWI to achieve high-resolution velocity models, with examples from the Sultanate of Oman. First, we demonstrated that with proper handling of the input data conditioning, a good acquisition geometry, and starting near-surface velocity model, we were able to obtain a stable high-frequency velocity model and the corresponding FWI image that substantially improves geologic understanding of the faulted structures and reduces exploration uncertainties. Second, as the use of a good near-surface model is important for stabilizing high-frequency FWI updates, we proposed using elastic FWI of surface waves to better deal with the strong elastic effects generated by complex shallow geology, as in the case study from the southern part of the Sultanate of Oman. Our approach benefits from the very energetic surface waves observed in this region, which require minimal preprocessing, and from the ultra-low frequencies recovered by interferometry to achieve a more stable and deeper update. We demonstrated the effectiveness of this workflow to enhance imaging of the shallow subsurface. The inverted V_S model could also be used for shallow-hazard and geotechnical studies. The examples presented here show that FWI is now becoming a key component in the velocity model building and imaging toolbox for land data. The natural next step for land FWI is to move toward full elastic FWI, which provides more correct physics to explain the recorded waves. Elastic FWI of surface waves can be used to create an S-wave near-surface velocity and a starting point for subsequent updates of V_P or other elastic parameters using not only surface but full elastic waves. TLE

Acknowledgments

We would like to thank Petroleum Development Oman, Shell, and the Ministry of Energy and Minerals of the Sultanate of Oman for permission to publish the data examples. We also thank our colleagues Nicolas Salaun and Todd Woodford for useful discussions and Viridien for permission to publish this work.

Data and materials availability

Data associated with this research are confidential and cannot be released.

Corresponding author: yonghe.guo@viridiengroup.com

References

Adwani, A., M. Danilouchkine, Q. Al-Siyabi, O. Al-Droushi, F. ten Kroode, R.-E. Plessix, and F. Ernst, 2022, Onshore model building using elastic full-waveform inversion on surface and body waves: A case study from Sultanate of Oman: Geophysics, **87**, no. 6, R413–R424, https://doi.org/10.1190/geo2021-0751.1.

Baeten, G., J. W. de Maag, R.-E. Plessix, R. Klaassen, T. Qureshi, M. Kleemeyer, F. ten Kroode, and Z. Rujie, 2013, The use of low frequencies in a full-waveform inversion and impedance inversion land seismic case study: Geophysical Prospecting, **61**, no. 4, 701–711, https://doi.org/10.1111/1365-2478.12010.

Bardainne, T., 2018, Joint inversion of refracted P-waves, surface waves and reflectivity: 80th Conference and Exhibition, EAGE, Extended Abstracts, https://doi.org/10.3997/2214-4609.201801158.

Borisov, D., R. Modrak, F. Gao, and J. Tromp, 2018, 3D elastic full-waveform inversion of surface waves in the presence of irregular topography using an envelope-based misfit function: Geophysics, **83**, no. 1, R1–R11, https://doi.org/10.1190/geo2017-0081.1.

Donno, D., M. S. Farooqui, M. Khalil, D. McCarthy, D. Solyga, J. Courbin, A. Prescott, L. Delmas, and D. Le Meur, 2021, Multi-wave inversion: A key step for depth model building — Examples from the Sultanate of Oman: The Leading Edge, **40**, no. 8, 610–618, https://doi.org/10.1190/tle40080610.1.

Espin, I., N. Salaun, H. Jiang, and M. Reinier, 2023, From FWI to ultra-high-resolution imaging: The Leading Edge, **42**, no. 1, 16–23, https://doi.org/10.1190/tle42010016.1.

Farooqui, M. S., D. Carotti, and M. Al-Jahdhami, 2021, Integrated high-resolution model building: A case study from the Sultanate of Oman: 82nd Conference and Exhibition, EAGE, Extended Abstracts, https://doi.org/10.3997/2214-4609.202112701.

Forbes, G. A., H. S. M. Jansen, and J. Schreurs, 2010, Lexicon of Oman subsurface stratigraphy: Gulf PetroLink.

Guillouet, M., A. Berthaud, T. Bianchi, G. Pignot, S. Mahrooqi, and J. Shorter, 2016, Recovery of blended data — A sparse coding approach for seismic acquisition: 78th Conference and Exhibition, EAGE, Extended Abstracts, https://doi.org/10.3997/2214-4609.201600947.

Guo, Y., and A. Aziz, 2024, New geological understanding with land FWI imaging, a Sultanate of Oman case study: 85th Conference and Exhibition, EAGE, Extended Abstracts, https://doi.org/10.3997/2214-4609.2024101107.

Hermant, O., A. Aziz, S. Warzocha, and M. Al Jahdhami, 2020, Imaging complex fault structures on-shore Oman using optimal transport full waveform inversion: 82nd Conference and Exhibition, EAGE, Extended Abstracts, https://doi.org/10.3997/2214-4609.202010734.

Huang, R., Z. Zhang, Z. Wu, Z. Wei, J. Mei, and P. Wang, 2021, Full-waveform inversion for full-wavefield imaging: Decades in the making: The Leading Edge, **40**, no. 5, 324–334, https://doi.org/10.1190/tle40050324.1.

Leblanc, O., A. Sedova, G. Lambaré, T. Allemand, O. Hermant, D. Carotti, D. Donno, and N. Masmoudi, 2022, Elastic land full-waveform inversion in the Middle East: Method and applications: 83rd Conference and Exhibition, EAGE, Extended Abstracts, https://doi.org/10.3997/2214-4609.202210375.

Le Meur, D., N. Benjamin, R. Cole, and M. Al Harthy, 2008, Adaptive ground-roll filtering: 70th Conference and Exhibition, EAGE, Extended Abstracts, https://doi.org/10.3997/2214-4609.20147745.

Le Meur, D., D. Donno, J. Courbin, D. Solyga, and A. Prescott, 2020, Retrieving ultra-low frequency surface waves from land blended continuous recording data: 90th Annual International Meeting, SEG, Expanded Abstracts, 1855–1859, https://doi.org/10.1190/segam2020-3418624.1.

Mahrooqi, S., S. Rawahi, S. Yarubi, S. Abri, A. Yahyai, M. Jahdhami, K. Hunt, and J. Shorter, 2012, Land seismic low frequencies — Acquisition, processing and full wave inversion of 1.5–86 Hz: 82nd Annual International Meeting, SEG, Expanded Abstracts, https://doi.org/10.1190/segam2012-0961.1.

Masclet, S., G. Bouquard, and H. Prigent, 2021, Multi-wave inversion and full-waveform inversion in southern Oman: 82nd Conference and Exhibition, EAGE, Extended Abstracts, https://doi.org/10.3997/2214-4609.202010731.

Messud, J., D. Carotti, O. Hermant, A. Sedova, and G. Lambaré, 2021, Optimal transport full-waveform inversion: From theory to industrial applications with examples from the Sultanate of Oman: First Break, **39**, no. 12, 45–53, https://doi.org/10.3997/1365-2397.fb2021090.

Ng, M., and M. Perz, 2004, High resolution radon transform in the t-x domain using "intelligent" prioritization of the Gauss-Seidel estimation sequence: 74th Annual International Meeting, SEG, Expanded Abstracts, 2160–2163, https://doi.org/10.1190/1.1845211.

Pérez Solano, C. A., D. Donno, and H. Chauris, 2014, Alternative waveform inversion for surface wave analysis in 2-D media: Geophysical Journal International, **198**, no. 3, 1359–1372, https://doi.org/10.1093/gji/ggu211.

Sedova, A., G. Royle, T. Allemand, G. Lambaré, and O. Hermant, 2019, High-frequency acoustic land full-waveform inversion: A case study from the Sultanate of Oman: First Break, **37**, no. 1, 75–81, https://doi.org/10.3997/1365-2397.n0010.

Sedova, A., O. Leblanc, M. Reinier, D. Donno, G. Lambaré, and D. Carotti, 2024, Near-surface characterization by elastic full-waveform inversion of surface waves: 85th Conference and Exhibition, EAGE, Extended Abstracts, https://doi.org/10.3997/2214-4609.2024101069.

Socco, L. V., and C. Strobbia, 2004, Surface-wave method for near-surface characterization: A tutorial: Near Surface Geophysics, **2**, no. 4, 165–185, https://doi.org/10.3997/1873-0604.2004015.

Sternfels, R., G. Viguier, R. Gondoin, and D. Le Meur, 2015, Multidimensional simultaneous random plus erratic noise attenuation and interpolation for seismic data by joint low-rank and sparse inversion: Geophysics, **80**, no. 6, WD129–WD141, https://doi.org/10.1190/geo2015-0066.1.

Stopin, A., R.-E. Plessix, and S. Al Abri, 2014, Multiparameter waveform inversion of a large wide-azimuth low-frequency land data set in Oman: Geophysics, **79**, no. 3, WA67–WA77, https://doi.org/10.1190/geo2013-0323.1.

Taillandier, C., M. Noble, H. Chauris, and H. Calandra, 2009, First arrival traveltime tomography based on the adjoint-state method: Geophysics, **74**, no. 6, WCB1–WCB10, https://doi.org/10.1190/1.3250266.

Virieux, J., and S. Operto, 2009, An overview of full-waveform inversion in exploration geophysics: Geophysics, **74**, no. 6, WCC1–WCC26, https://doi.org/10.1190/1.3238367.

Wang, P., Z. Zhang, J. Mei, F. Lin, and R. Huang, 2019, Full-waveform inversion for salt: A coming of age: The Leading Edge, **38**, no. 3, 204–213, https://doi.org/10.1190/tle38030204.1.

Zhang, Z., Z. Wu, Z. Wei, J. Mei, R. Huang, and P. Wang, 2020, FWI imaging: Full-wavefield imaging through full-waveform inversion: 90th Annual International Meeting, SEG, Expanded Abstracts, 656–660, https://doi.org/10.1190/segam2020-3427858.1.

Zhao, J., H. Jin, Y. Zhu, Y. C. El-Taha, and F. Clow, 2018, Vibroseis ultra high productivity blended acquisition: Field trial and full scale implementation in Oman: International Geophysical Conference, Extended Abstracts, 150–153, https://doi.org/10.1190/IGC2018-038.